

# Weakly-supervised segmentation using inherently-explainable classification models and their application to brain tumour classification

Soumick Chatterjee<sup>a,b,c,\*</sup>, Hadya Yassin<sup>d,\*</sup>, Florian Dubost<sup>e</sup>, Andreas Nürnberger<sup>a,f</sup>, Oliver Speck<sup>b,f,g</sup>

<sup>a</sup>Data and Knowledge Engineering Group, Faculty of Computer Science, Otto von Guericke University Magdeburg, Germany

<sup>b</sup>Biomedical Magnetic Resonance, Faculty of Nature Sciences, Otto von Guericke University Magdeburg, Germany

<sup>c</sup>Genomics Research Centre, Human Technopole, Milan, Italy

<sup>d</sup>Institute for Medical Engineering, Faculty of Electrical Engineering and Information Technology, Otto von Guericke University Magdeburg, Germany

<sup>e</sup>Department of Biomedical Data Science, Stanford University, Stanford, CA, United States

<sup>f</sup>Centre for Behavioural Brain Sciences, Magdeburg, Germany

<sup>g</sup>German Centre for Neurodegenerative Disease, Magdeburg, Germany

## Abstract

Deep learning models have shown their potential in recent years for several applications. However, most of the models are opaque in nature and difficult to trust due to their complex reasoning - commonly known as the black-box problem. Some fields, such as medicine, require a high degree of transparency to accept and adopt such technologies. Consequently, there is a movement towards creating explainable/interpretable models or applying post-hoc explainability/interpretability methods on classifiers to build trust in deep learning models. Moreover, deep learning methods can be used for segmentation tasks, which typically require hard-to-obtain, time-consuming manually-annotated segmentation labels for training. This paper introduces three inherently-explainable classifiers to tackle both of these problems as one. The localisation heatmaps provided by the networks – representing the models’ focus areas and being used in classification decision-making – can be directly interpreted, without requiring any post-hoc methods to derive information for model explanation. The models are trained by using the input image and only the classification labels as ground-truth in a supervised fashion - without using any information about the location of the region of interest (i.e. the segmentation labels), making the segmentation training of the models weakly-supervised through classification labels. The final segmentation of the regions of interest is obtained by thresholding these heatmaps. The models were employed for the task of multi-class brain tumour classification using two different datasets, resulting in the best F1-score of 0.93 for the supervised classification task while securing a median Dice score of  $0.67 \pm 0.08$  for the weakly-supervised segmentation task. Furthermore, the obtained accuracy on a subset of tumour-only images outperformed the state-of-the-art glioma tumour grading binary classifiers with the best model achieving 98.7% accuracy.

**Keywords:** Brain tumour, Classification, Segmentation, Explainable AI, Convolutional neural network, Magnetic Resonance Imaging

## 1. Introduction

Convolutional neural networks (CNN) are widely used in image processing, including in the medical field. Although CNNs conducted in a supervised manner have shown significant outcomes in disease classification tasks, traditional means are still the go-to method for diagnosis, such as histopathological analysis of biopsy specimens to classify and diagnose brain tumours (Noor et al., 2019; Irmak, 2021). A biopsy procedure is invasive, time-consuming, and susceptible to manual errors. Early detection of tumours is crucial for the survival of the patient, and therefore an automated deep-learning method might offer a better solution and overcome the disadvantages above. While early detection and appropriate diagnosis are critical for a patient’s survival, segmenting the tumour for further inspection and monitoring of the disease’s progression, as well as aiding in the treatment process, is also necessary.

Some critical issues must be addressed before deep learning methods can be widely accepted and adopted in the medical field. Because of the complexity of the CNNs reasoning process, they tend to be obscure and are frequently referred to as black boxes. While some researchers came up with post-hoc methods to explain and interpret such models (Chatterjee et al., 2022b), (Kenny et al., 2021), (Laugel, 2020), (Madsen et al., 2021), others try to create inherently explainable-interpretable models. Additionally, most deep learning based segmentation models are based on supervised learning and require manually annotated data, which is time-consuming and imposes a big challenge. Nevertheless, labelling the data with the type of tumour or whether it is present or not is much easier for radiologists and, hence, less time-consuming. Dubost et al. (2017) has shown the potential of training a segmentation model in a weakly-supervised manner using regression labels for lesion counts. This research aims to develop fully automated, inherently explainable CNN models for brain tumour multi-class classification, which are also capable of tumour segmentation

\*S. Chatterjee and H. Yassin have Equal Contribution

without the need for segmentation labels.

### 1.1. Related Work

Several deep learning models have been proposed for the task of brain tumour classification and segmentation, while some models address both problems in a unified fashion.

#### 1.1.1. Classification Models

Without any prior region-based segmentation, Abiwinanda et al. (2019) applied the most straightforward possible architecture of CNN on the brain tumour dataset with a validation accuracy of 84.19% at best. Sultan et al. (2019) proposed a CNN architecture for classifying brain cancers into the three classes of tumours in the brain tumour dataset, as well as distinguishing between the three glioma categories (Grade II, Grade III, and Grade IV). Badža and Barjaktarović (2020) created a 22-layered CNN architecture for brain tumour type classification. Ayadi et al. (2021) proposed a CNN-based computer-assisted diagnosis (CAD) system using an 18-weighted layered CNN model for brain classification on two distinct datasets.

As for models based on transfer learning, Khawaldeh et al. (2018) developed a modified version of the AlexNet CNN model to classify brain MRI images into healthy, low-grade glioma and high-grade glioma. Deepak and Ameer (2019) employed a pre-trained GoogleNet CNN model to distinguish between the three types of tumours. Rehman et al. (2020) proposed using three pre-trained CNN models known as AlexNet, GoogleNet, and VGG16 to classify tumours in the brain tumour dataset.

#### 1.1.2. Segmentation Models

Pereira et al. (2016) developed a 3x3 kernels-based CNN and yielded 88%, 83%, 77% dice coefficients in the BraTS 2013 challenge for complete, core, and enhancing tumour, respectively. They won second place in the BraTS 2015 challenge with a Dice coefficient of 78%, 65%, and 75%. Razzak et al. (2018) presented a new model two-pathway-group CNN architecture for brain tumour segmentation that concurrently uses local and global contextual data. They include the cascade design into a two-pathway-group CNN, in which the output of a basic CNN is considered a second source and concatenated at the final layer. Cascade CNN was Superior to the CNN alone and yielded 88.9%, 81.1%, 73.7% dice coefficients on the BraTS 2013 dataset for complete, core, and enhancing tumours, respectively. They also achieved 89.2%, 79.18%, 75.1% dice coefficients on the BraTS 2015 dataset (Razzak et al., 2018). Li et al. (2019) proposed a novel CNN based on UNet, which improves information flow in the network by using a unique structure called an up-skip connection between the encoding and decoding paths. Furthermore, each block includes an inception module to aid the network in learning richer representations in addition to effective cascade training techniques for successively segmenting brain tumour subregions. The model scores a dice value of 89% for the complete tumour of the BraTS 2017 dataset (Li et al., 2019).

#### 1.1.3. Combined Models

Dubost et al. (2017) developed a novel convolutional neural network, which serves as the baseline for this work. The network is an UNet based 3D regression network that detects lesions from weak labels. They achieved a sensitivity of 62% with an average of 1.5 false positives per image by combining a lesion count regression task with lesion detection in one model, where only a single label per image (lesion count) is required for training (Dubost et al., 2017). Díaz-Pernas et al. (2021) developed a tumour classification and segmentation model based on pixel-wise classification into four classes, including healthy, meningioma, glioma, and pituitary tumour. This method was trained and tested on the brain tumour dataset achieved 5-fold cross-validation average values of 94% for classification sensitivity and 0.82 for segmentation dice coefficient. Additionally, they scored a 97.3% classification accuracy.

## 2. Methodology

### 2.1. Network Models

The proposed CNNs are based on modified segmentation or reconstruction models - modified to work as a multi-class classifier with only one global class label per image. The original models generate  $n$  equally sized output images with the same size as the input, where  $n$  is the number of segmentation classes that were required. In this proposed approach, prior to applying the final fully-connected convolution layer, the modified CNN network is coupled with a global pooling layer in the training stage to aggregate the 3D output into a single-pixel (neuron) for each class. As a result, classification image-level labels work for training the model in a supervised manner, as an alternative to the traditional cumbersome segmentation labels during the network's training - making the segmentation training of the network weakly-supervised. During the testing stage, the global pooling layer can be removed to obtain the heatmaps with the same size as the input, or it can be kept as in the training stage to obtain the class. The obtained heatmaps show the region-of-interest of the network - portraying the network's focus area - making the network inherently explainable. The resulting heatmaps are then suppressed by setting the negative values to zero. Without using any post-hoc interpretability methods, the model's focus areas can be understood simply by glancing at the heatmaps. Afterwards, the segmentation mask is created using Otsu thresholding. The general overview of the models is shown in Fig. 1.

Three different segmentation/reconstruction models were explored in this research: UNet (Ronneberger et al., 2015) - which was also used by Dubost et al. (2017), ReconResNet (Chatterjee et al., 2022a), and ShuffleUNet (Chatterjee et al., 2021), to construct GP-UNet, GP-ReconResNet, and GP-ShuffleUNet, respectively. The resultant network architectures are shown in Figures 2, 3, and 4, respectively. Original U-Net and ShuffleUNet models were modified by adding a dropout layer with a probability of 0.5 in the GP-models to avoid overfitting, whereas probability of the dropout layer which is already implemented in ReconResNet was increased to 0.5. The proposed

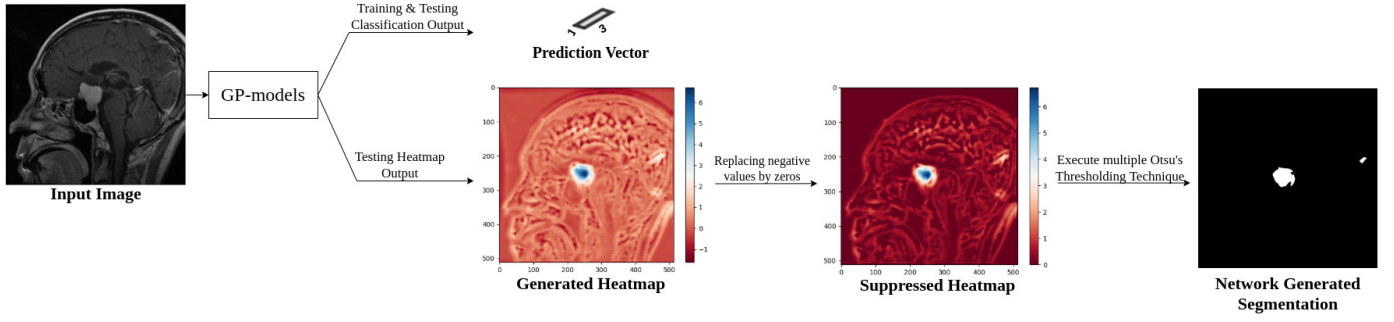


Figure 1: Workflow of the GP-models

Table 1: Number of parameters and training time for each model.

Model Name	No. of Parameters	Training Time
InceptionV3	21.8 M	~ 2 day
ResNext50	23.0 M	~ 2 day
GP-UNet	1.90 M	~ 4 days
GP-ShuffleUNet	26.4 M	~ 13 days
GP-ReconResNet	17.3 M	~ 9 days

GP-models were compared against two non-GP models: InceptionV3 (Szegedy et al., 2016) and ResNeXt50 (Xie et al., 2017), which were chosen by comparing the performance of various other models. Table 1 shows the number of parameters and the approximate training time.

## 2.2. Implementation

The implementation was done using PyTorch and PyTorch-lightning, and the experiments were performed using an Nvidia GeForce RTX 2080 TI GPU. The data was partitioned into three sets: training, validation, and testing, with real-time spatial augmentation during the training phase. The networks were trained with the help of automatic mixed-precision for 300 epochs for the second dataset, with various batch sizes, depending on when each model converged and how large it was memory-wise, keeping the effective batch size as 128 by accumulating gradients of multiple batches before backpropagating. The loss was calculated using the weighted cross-entropy loss function and was optimised using the Adam optimiser with a learning rate of 0.001. To avoid overfitting, along with adding dropout layers inside the network models, L2 regularisation weights decay factor of  $5e-4$  was also employed. To avoid exploding gradients, a gradient clip-off value of one was applied. Finally, post-hoc interpretability methods (Chatterjee et al., 2022b) were applied to all GP and non-GP models - to be able to compare their interpretability. The code of this research is publicly available on GitHub <sup>1</sup>.

## 2.3. Dataset

The network models were employed for the task of brain tumour classification using two different datasets. The first

dataset (Jun Cheng) contains 3,064 2D T1-weighted contrast-enhanced MRI slices from 233 patients with three types of brain tumours: meningioma (708 slices), glioma (1426 slices), and pituitary tumour (930 slices), in three different orientations: axial (993 slices), coronal (1046 slices), and sagittal (1025 slices). The second dataset used in this research is the BraTS 2020 dataset (Menze et al., 2014; Lloyd et al., 2017; Bakas et al., 2018). This dataset contains multimodal scans acquired with different clinical protocols and scanners from 19 institutions of 346 patients with two different types of tumours: low-grade glioma (LGG, 73 patients) and high-grade glioma or glioblastoma (HGG, 273 patients), each having 3D volumes of T1-weighted (T1w), post-contrast T1-weighted (T1ce), T2-weighted (T2), and T2 Fluid Attenuated Inversion Recovery (T2-FLAIR, or simply, FLAIR) MRIs in axial orientation - a total of  $4 \times 47,686$  slices after ignoring blank slices. The slices without any tumour were considered as "tumour-free" and a third class was created using them, resulting in 4,731, 18,276, and 24,679 slices, for LGG, HGG, and tumour-free class, respectively. The images were manually segmented by one to four raters, and the annotations were agreed upon by neuro-radiology experts. All four types of MRIs were concatenated on the channel dimension and were supplied to the networks in 2D, slice-wise manner. The four-channel approach was inspired by the belief that different contrasts provide varying degrees of diagnosis strength and assurance. In a sense, the entire tumour or parts of it might appear clearer to the human eye and achieve greater evaluation results using one contrast versus the other (Jeong et al., 2014). Three fold cross-validation was performed by randomly creating subsets with the ratio of 60:15:25 using stratified sampling for training, validation, and testing, respectively.

### 2.3.1. Augmentation

Table 2 illustrates the real-time augmentation techniques performed only on the training set, in which each image in the set is randomly rotated in the range of  $-330$  to  $+330$ , horizontally or vertically flipped, each with a 50% chance of occurring independently from one another. Augmentation can be proven helpful to prevent overfitting and enhance model robustness (Krizhevsky et al., 2012; Wong et al.).

<sup>1</sup>Code on GitHub: <https://github.com/soumickmj/GPModels>

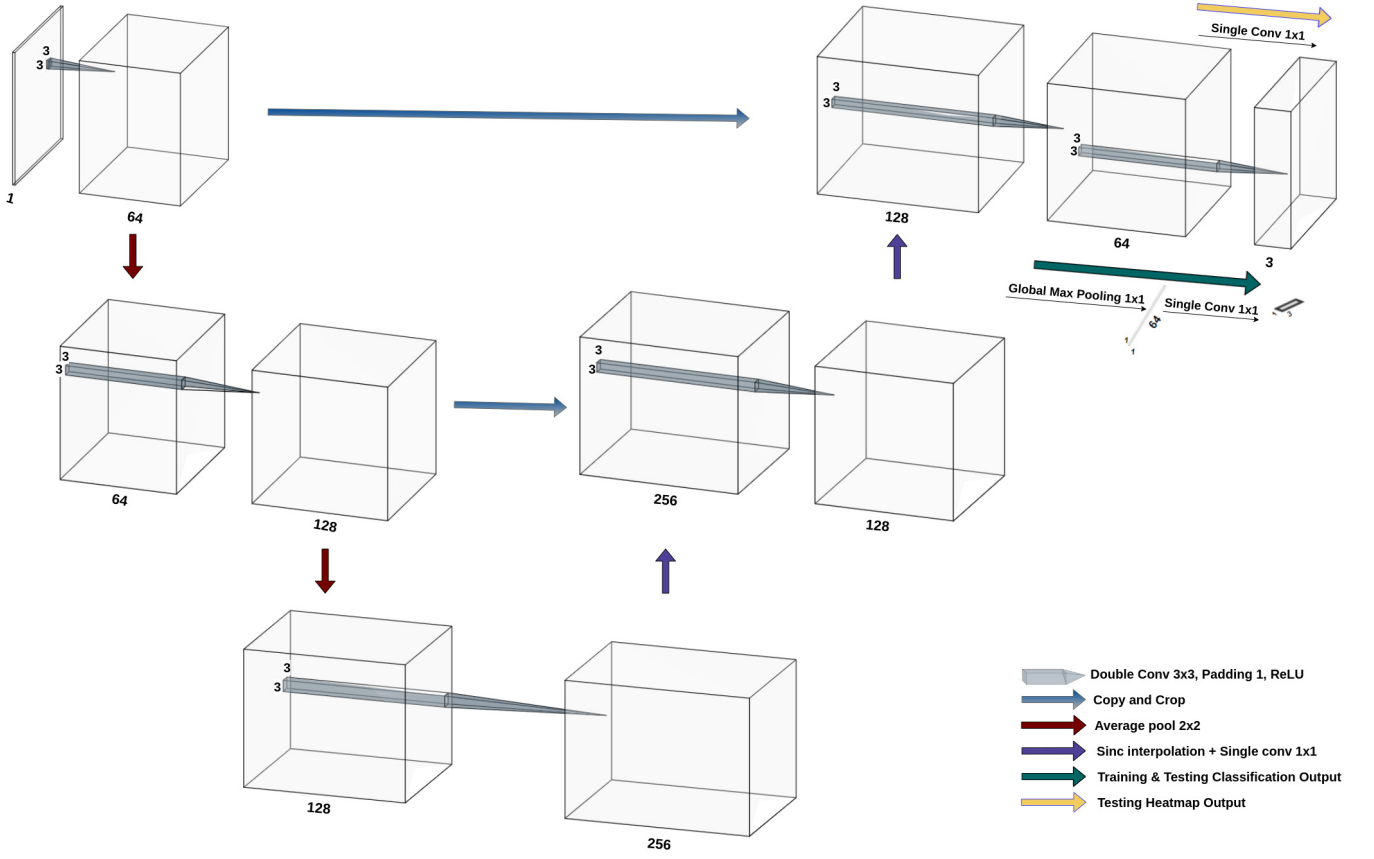


Figure 2: The original Network Architecture of the baseline GP-UNet model(Dubost et al., 2017) was modified by changing the up-pooling mechanism from transposed-convolution to interpolation+convolution (Sinc Up-sample method) and changing the output convolution filter number from  $2^{5+i}$  to  $2^{6+i}$ ,  $i = 0, 1, 2$  corresponding to the original depth of the model (depth=3). A dropout layer with a probability value of 0.5 was added to the model during training.

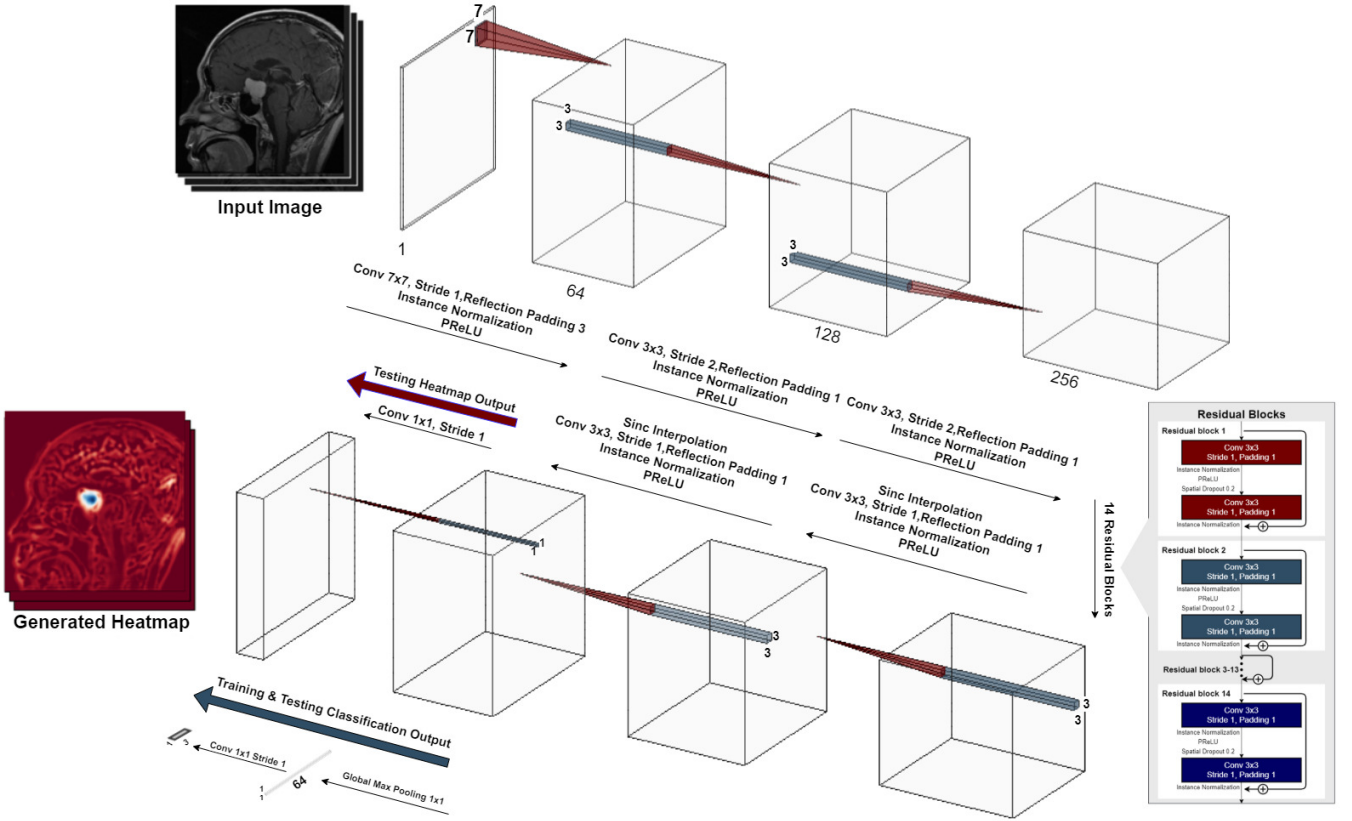


Figure 3: The Network Architecture of the proposed GP-ReconResNet model. When training and testing on the BraTS 2020 dataset, a dropout layer with a probability value of 0.5 instead of 0.2 was used in the model.

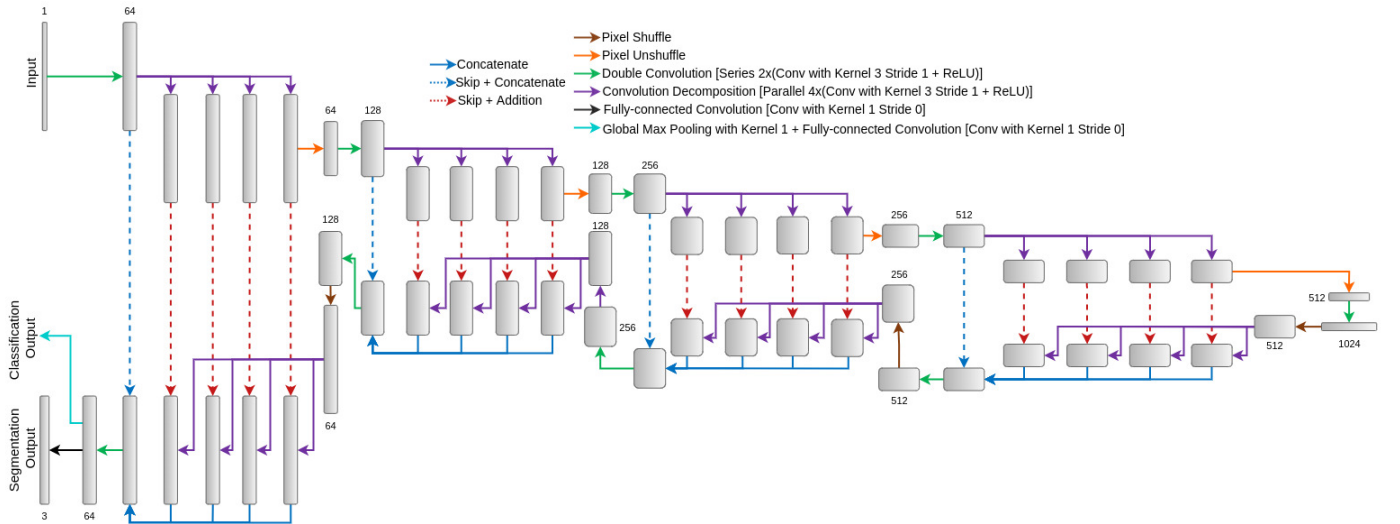


Figure 4: The Network Architecture of the proposed GP-ShuffleUNet model (Chatterjee et al., 2021). The original model was altered by adding a global pooling layer before the fully connected convolution in the training stage transforming the model to a GP-Model, while also adding a dropout layer with a probability value of 0.5.

Table 2: The applied spatial augmentation techniques and their respective parameters.

Methods	Parameter
Flip horizontally	50% probability
Flip vertically	50% probability
Rotation	$\pm 330^\circ$

#### 2.4. Evaluation Criteria

The F1-score was used as the primary quantitative metric for evaluating the models’ classification performance. When having similar F1 scores, other measures such as confusion matrix, accuracy, recall, and precision were employed to quantify the results. To account for data imbalance in the BraTS dataset, a weighted average of the matrix values was used. The Dice similarity coefficient was used as a quantitative metric assessing the GP-models’ segmentation performance. As for the last aspect, the model’s inherent explainability and transparency were assessed by visually inspecting the generated localisation heatmaps, revealing the models’ classification decision basis. Furthermore, post-hoc interpretability methods were applied to the best performing GP- and non-GP- models to be able to compare interpretability aspects in both.

### 3. Results

For the first set of experiments with the first dataset (Jun Cheng), trainings were performed by supplying individual 2D slices of T1ce MRIs as single-channel input to the network models and were trained to perform 3-class classification for the type of brain tumour: meningioma, glioma, and pituitary tumour. For the second set of experiments with the BraTS dataset (Menze et al., 2014; Lloyd et al., 2017; Bakas et al., 2018), trainings were performed by concatenating the four multi-modal MRIs: T1, T1ce, T2, and Flair on the channel-dimension, and were trained for 3-class classification for tumour-free and two different types of brain tumours - LGG and HGG. It is worth mentioning that both datasets are imbalanced, whereas the second dataset is much more imbalanced compared to the first one. The number of slices in the first dataset has a ratio of 23:30:47 for meningioma:pituitary:glioma classes, while the ratio in the second dataset was 10:38:52 for LGG:HGG:tumour-free classes. Even though the first dataset poses less challenge in terms of class imbalance, it provides two different challenges: it is considerably smaller and contains a mix of three orientations, while the second dataset is much larger and contain only MRIs acquired in axial orientation. The models were initially evaluated for their classification performance, followed by their segmentation performance. Finally, additional evaluations were performed with the interpretability techniques.

#### 3.1. Experiments with Dataset #1

Table 3 shows the quantitative results for the different GP-models and the non-GP baseline models. The GP-ReconResNet

Table 3: Resulting classification metrics (Precision, Recall, F1-score, Accuracy) for all the models, and the segmentation metrics (median Dice score) for the GP-models, on the first dataset (Jun Cheng)

Model Name	Precision	Recall	F1-Score	Accuracy	Med (DSC)
InceptionV3	0.96	0.97	0.97	0.97	-
ResNext50	0.96	0.96	0.96	0.97	-
GP-ReconResNet	0.96	0.95	0.95	0.95	$0.10 \pm 0.0365$
GP-ShuffleUNet	0.94	0.92	0.93	0.93	$0.04 \pm 0.0069$
GP-UNet	0.86	0.85	0.85	0.85	$0.05 \pm 0.0115$

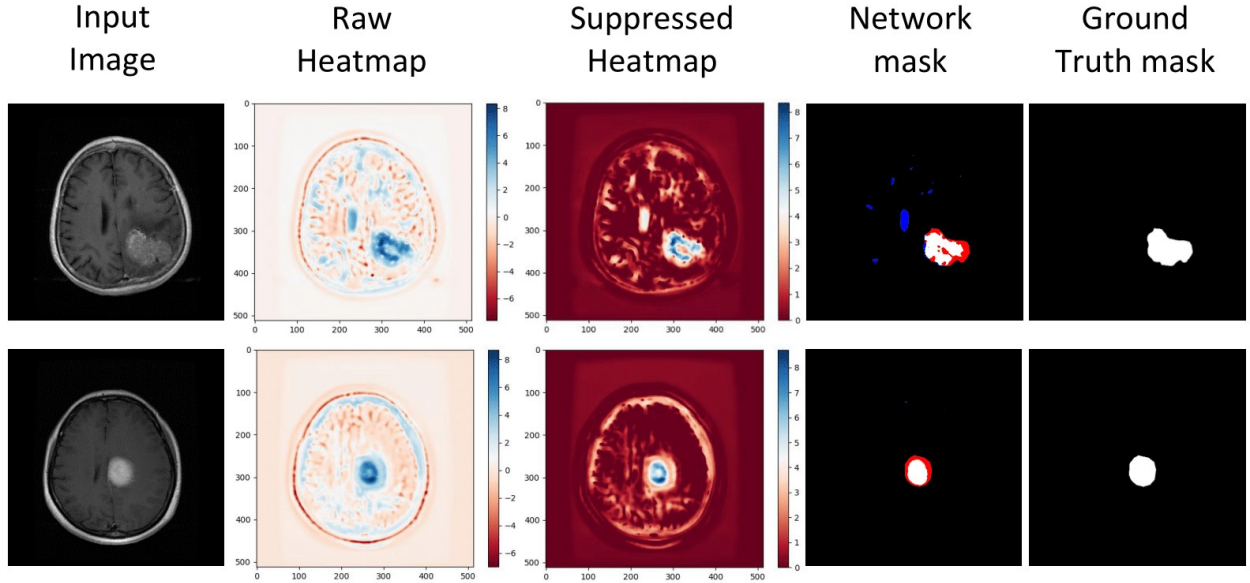
performed the best among the GP-models, scoring an F1-score of 0.95, while the GP-UNet and GP-ShuffleUNet secured the second and third positions, respectively, with 0.85 and 0.82 F1-scores. Fig. 5 shows a few examples of the segmentation in all three orientations for the GP-ReconResNet. It can be observed that the heatmap shows the tumour appropriately localised, and the post-processing helped in obtaining the segmentations.

#### 3.2. Experiments with Dataset #2: BraTS 2020 dataset

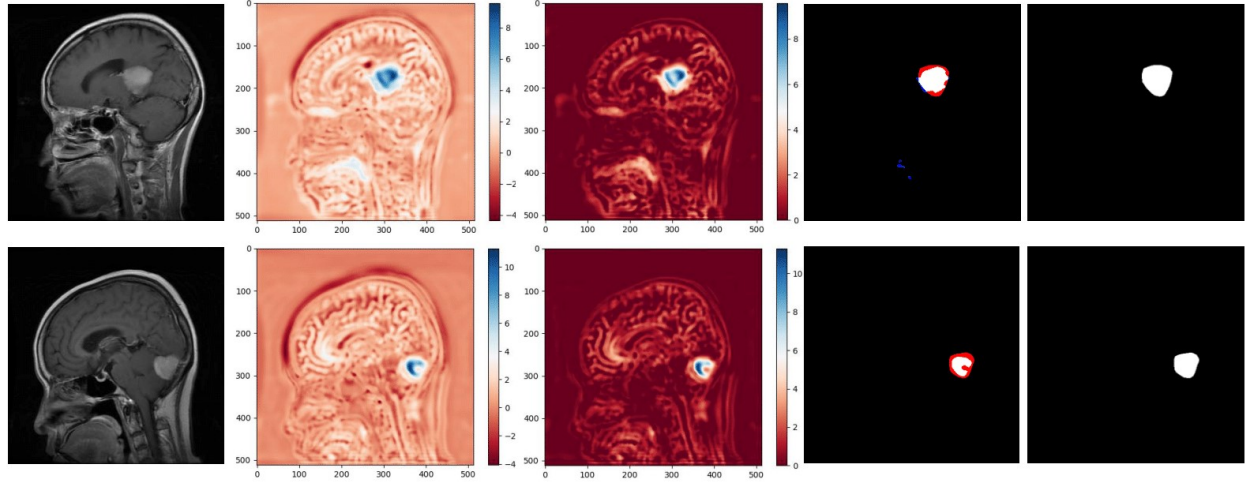
On the BraTS dataset, the models show a different trend compared to the first dataset. GP-UNet and GP-ShuffleUNet resulted in 0.93 F1-score, while GP-ReconResNet resulted in 0.92. In terms of accuracy, GP-ShuffleUNet got 0.94, while GP-UNet and GP-ReconResNet both obtained 0.93. However, both the non-GP baselines resulted in 0.95 F1-score and accuracy. Even though the non-GP models resulted in better scores, it is worth mentioning that the non-GP models are not inherently explainable and do not assist in producing segmentations as the GP-models. Table 4 shows the complete results on different metrics. The classification performance of these models was further shown using confusion matrices in Fig. 7. The accuracy on a subset of the test set considering only the slices for the two tumour classes for the GP-models were compared against other state-of-the-art methods which also have used the BraTS dataset (but different versions), and it can be seen that the GP-models outperform all the other methods, while also being inherently explainable - shown in Table 5. The reason behind considering only LGG and HGG classes in this analysis was that the compared methods only have considered these classes in their analyses. It is to be noted, though, that the methods that worked with 3D volumes included the tumour-free slices - part of the volumes but classified the whole volume as LGG or HGG class.

Coming to the segmentation performance, the Dice scores show a little different trend than the classification scores, shown in Table 4. Two different methods were used for generating the final segmentation masks from the heatmaps: multi-Otsu thresholding with an offset and a fixed threshold of 0.5. While for the GP-UNet and GP-ShuffleUNet the first approach resulted in better segmentation, for GP-ReconResNet the second approach worked better. Hence for GP-ReconResNet, both results are furnished, denoted as GP-ReconResNet<sub>1</sub> and GP-ReconResNet<sub>2</sub>, respectively for the two approaches. In terms of the segmentation performance, GP-UNet secured the first position among the GP-models, scoring a median Dice of  $0.67 \pm 0.08$ , while the GP-ReconResNet segmentation (GP-

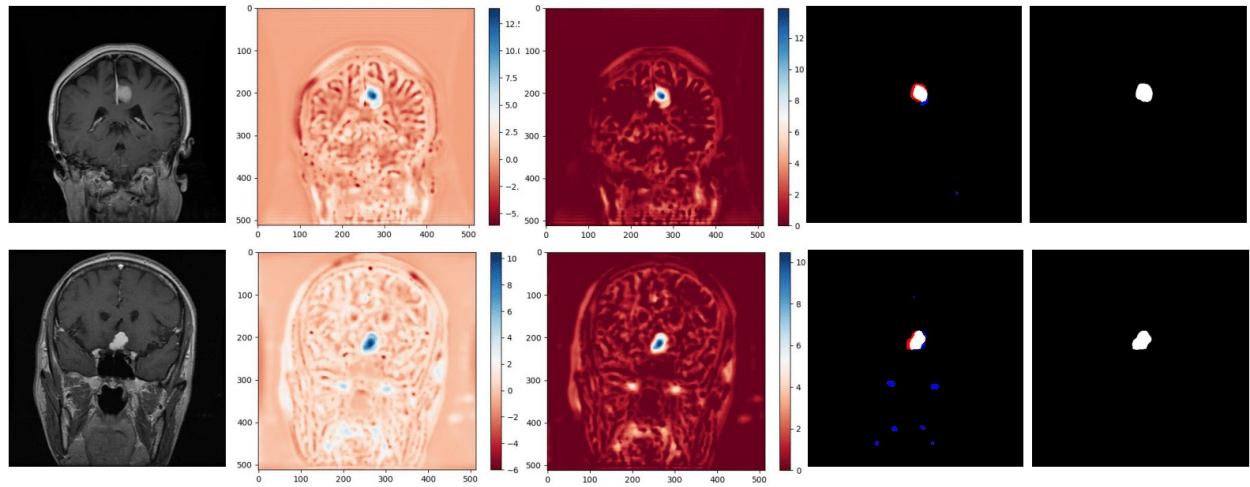




a) Axial Orientation



b) Sagittal Orientation



c) Coronal Orientation

Figure 5: Example results of the best-performing GP-ReconResNet on the 1st Dataset (Jun Cheng), in a) Axial, b) Sagittal and c) Coronal orientations. 1st column contains the input slices. 2nd column contains the model's prediction known as the raw heatmaps, where the red areas influenced the classification outcome negatively, and the blue areas influenced the classification outcome favourably. 3rd column contains the suppressed heatmaps, where negative values are suppressed to obtain positive attributions only. 4th column contains the network generated final masks = the suppressed heatmap + Otsu thresholding. The mask is then compared to the ground-truth mask, where white indicates true segmentation, blue indicates over-segmentation, and red indicates under-segmentation. 5th column contains the ground truth mask.

Table 4: Resulting classification metrics (Precision, Recall, F1-score, Accuracy) for all the models, and the segmentation metrics (median Dice score) for the GP-models, on the BraTS 2020 dataset.

Model Name	Precision	Recall	F1-Score	Accuracy	Dice score
InceptionV3	0.95	0.95	0.95	0.95	-
ResNeXt50	0.95	0.95	0.95	0.95	-
GP-UNet	0.93	0.93	0.93	0.93	$0.67 \pm 0.08$
GP-ShuffleUNet	0.94	0.94	0.93	0.94	$0.53 \pm 0.08$
GP-ReconResNet <sub>1</sub>	0.93	0.93	0.92	0.93	$0.50 \pm 0.07$
GP-ReconResNet <sub>2</sub>	0.93	0.93	0.92	0.93	$0.60 \pm 0.06$

Table 5: Comparison of the proposed GP-models with the previously published non-deep learning (non-DL) and deep learning (DL) works (<sup>†</sup> cross-validated) for the BraTS dataset.

Study / Model	Contrast	Model Type	Explainable	Test Accuracy
Latif et al. (2017)	T1, T1ce, T2, T2-FLAIR	non-DL 3D	N	88.31 %
Cho and Park (2017)	T1, T1ce, T2, T2-FLAIR	non-DL 3D	N	89.81% <sup>†</sup>
Shahzadi et al. (2018)	T1, T2, T2-FLAIR	DL 3D	N	84.00 %
Ge et al. (2018)	T1, T2, T2-FLAIR	DL 2D	N	90.87%
Yang et al. (2018)	T1ce	DL 2D	N	94.50% <sup>†</sup>
Mzoughi et al. (2020)	T1ce	DL 3D	N	96.49%
Zhuge et al. (2020)	T1, T1ce, T2, T2-FLAIR	DL 3D	N	97.10%
Chatterjee et al. (2022c)	T1ce	DL 3D	N	96.98% <sup>†</sup>
Barstugan (2023)	T1, T1ce, T2	non-DL 3D	Y	90.17% <sup>†</sup>
Hafeez et al. (2023)	T1, T1ce, T2, T2-FLAIR	DL 2D	N	97.15%
Dutta et al. (2024)	T1, T1ce, T2, T2-FLAIR	DL 2D	N	96.87% <sup>†</sup>
<b>GP-UNet</b>	<b>T1, T1ce, T2, T2-FLAIR</b>	<b>DL 2D</b>	<b>Y</b>	<b>98.27%<sup>†</sup></b>
<b>GP-ShuffleUNet</b>	<b>T1, T1ce, T2, T2-FLAIR</b>	<b>DL 2D</b>	<b>Y</b>	<b>98.74%<sup>†</sup></b>
<b>GP-ReconResNet</b>	<b>T1, T1ce, T2, T2-FLAIR</b>	<b>DL 2D</b>	<b>Y</b>	<b>97.99%<sup>†</sup></b>

ReconResNet<sub>2</sub>) obtained  $0.60 \pm 0.06$  and GP-ShuffleUNet obtained  $0.53 \pm 0.08$ . The resulting Dice scores have been visualised using histograms in Fig. 6. Figures 8 and 9 show the generated heatmaps and the segmentation results of the GP-models, for LGG and HGG classes, respectively.

### 3.3. Post-hoc interpretability

The GP-models presented here are explainable by nature, giving them an advantage over the competition in terms of model transparency and explainability portrayed. The focus area of the network can be understood from the generated heatmaps by those GP-models. The non-GP baselines are not explainable or interpretable, and typically post-hoc interpretability methods can be applied to understand the focus area of those networks (Chatterjee et al., 2020). Therefore, two interpretability methods, one feature-based model attribution technique - occlusion, and one gradient-based model attribution technique - guided backpropagation, were applied to all the models to generate the interpretability results using the TorchEsegeta pipeline (Chatterjee et al., 2022b). Figures 10 and 11 show the interpretability results for all the five models, for LGG

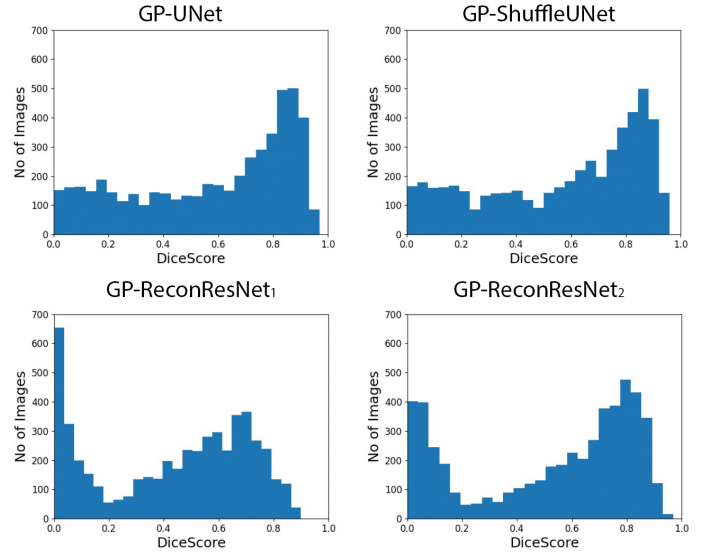


Figure 6: Histogram plots displaying the distribution of the Dice scores for the segmentation results of each of the GP-models on the BraTS 2020 dataset, namely GP-UNet after an Otsu thresholding with an offset of 0.3, GP-ShuffleUNet after an Otsu thresholding with an offset of 0.1, GP-ReconResNet<sub>1</sub> after an Otsu thresholding with an offset of 1.6 and GP-ReconResNet<sub>2</sub> with a fixed threshold of 0.5.

and HGG, respectively. As the GP-models are inherently explainable, the resultant heatmaps are also compared against the interpretability results.

For the GP-models, by comparing the heatmaps against the interpretability results, it can be said that the interpretability results do agree with the heatmaps. The occlusion results show that the GP-models focused on the tumour. For GP-ReconResNet however, some questionable results can be seen. For LGG class, some negative attributions can be seen in the bottom side of the tumour, while for HGG class, the focus is scattered in different parts of the brain - but missing parts of the tumour, which is shown as the most important focus region according to the heatmap. Guided backpropagation has also shown the centre of the focus area(s) of the network, and they agree with the heatmaps. However, the area covering the attribution is considerably smaller than occlusion, as well as the heatmaps. This analysis shows that the interpretability results can be trusted, but might be considered with caution.

The interpretability results of the non-GP baselines show that the reasoning done by the ResNeXt50 model is better than the InceptionV3, even though they both have secured the same classification scores. The positive, as well as the negative attributions for the InceptionV3, are scattered nearly all over the brain.



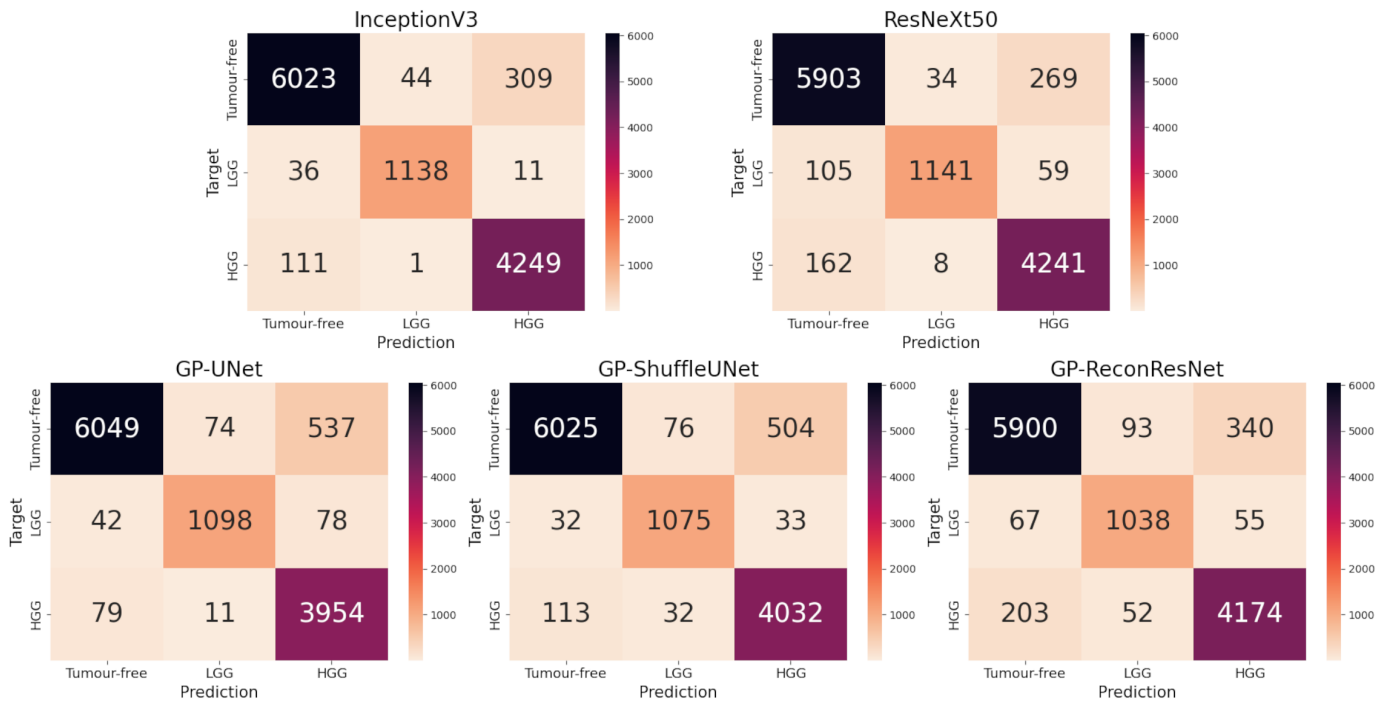


Figure 7: Confusion matrices of the GP- and non-GP- models, where the three classification labels depicted as HGG for high-grade glioma (glioblastoma), LGG for low-grade glioma, and tumour-free.

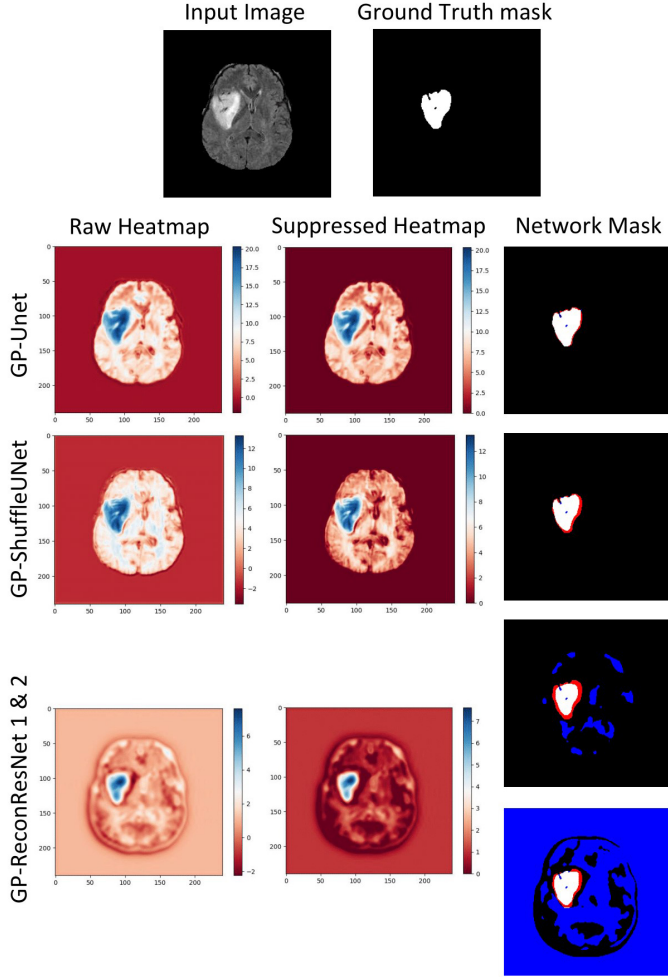


Figure 8: Example results of the GP-models' correctly classified LGG tumour (class 1) from the BraTS 2020 dataset. 1st row is the input slice, the ground truth mask is used for comparison, and the rest of the rows are the models' outputs. For the rest of the rows: 1st column contains the models' predictions known as the raw heatmaps, where the red areas influenced the classification outcome negatively, and the blue areas influenced the classification outcome favourably; 2nd column contains the suppressed heatmaps, where negative values are suppressed to obtain positive attributions only; 3rd column contains the networks' generated final masks = the suppressed heatmap + thresholding.

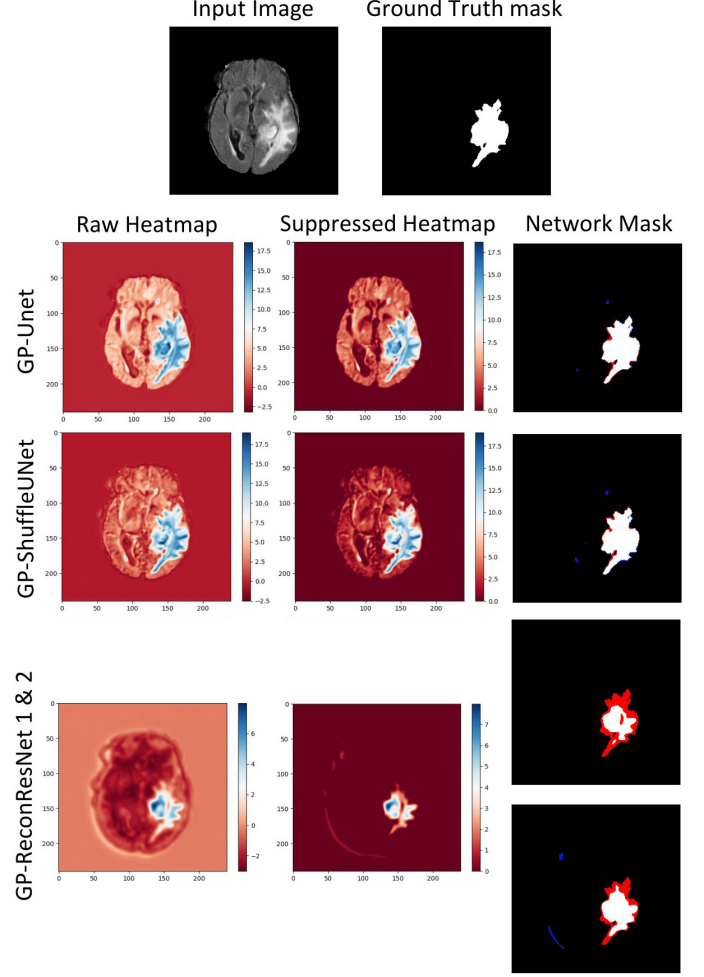


Figure 9: Example results of the GP-models' correctly classified HGG tumour (class 2) from the BraTS 2020 dataset. 1st row is the input slice, the ground truth mask is used for comparison, and the rest of the rows are the models' outputs. For the rest of the rows: 1st column contains the models' predictions known as the raw heatmaps, where the red areas influenced the classification outcome negatively, and the blue areas influenced the classification outcome favourably; 2nd column contains the suppressed heatmaps, where negative values are suppressed to obtain positive attributions only; 3rd column contains the networks' generated final masks = the suppressed heatmap + thresholding.

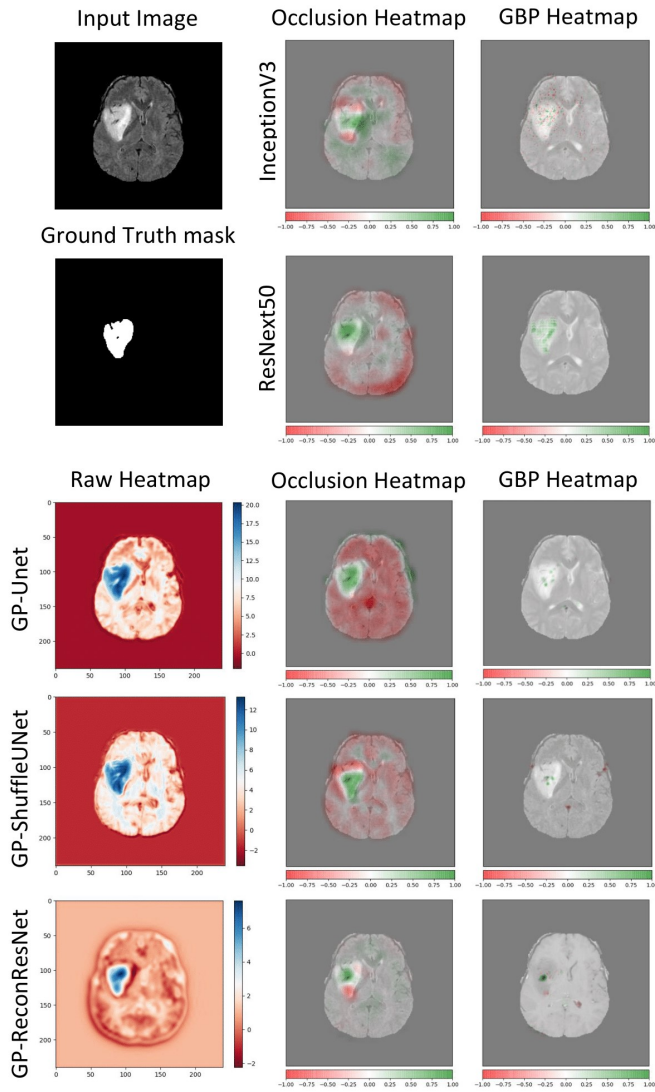


Figure 10: Example interpretability results of the GP- and non-GP models, correctly classified LGG (class 1). 1st column contains the input image, ground-truth mask, and the raw heatmaps of the GP-models. 2nd and 3rd columns contain the post-hoc interpretability attributions using the occlusion and the guided backpropagation (GBP) methods, respectively - overlaid as heatmaps on the input slices.

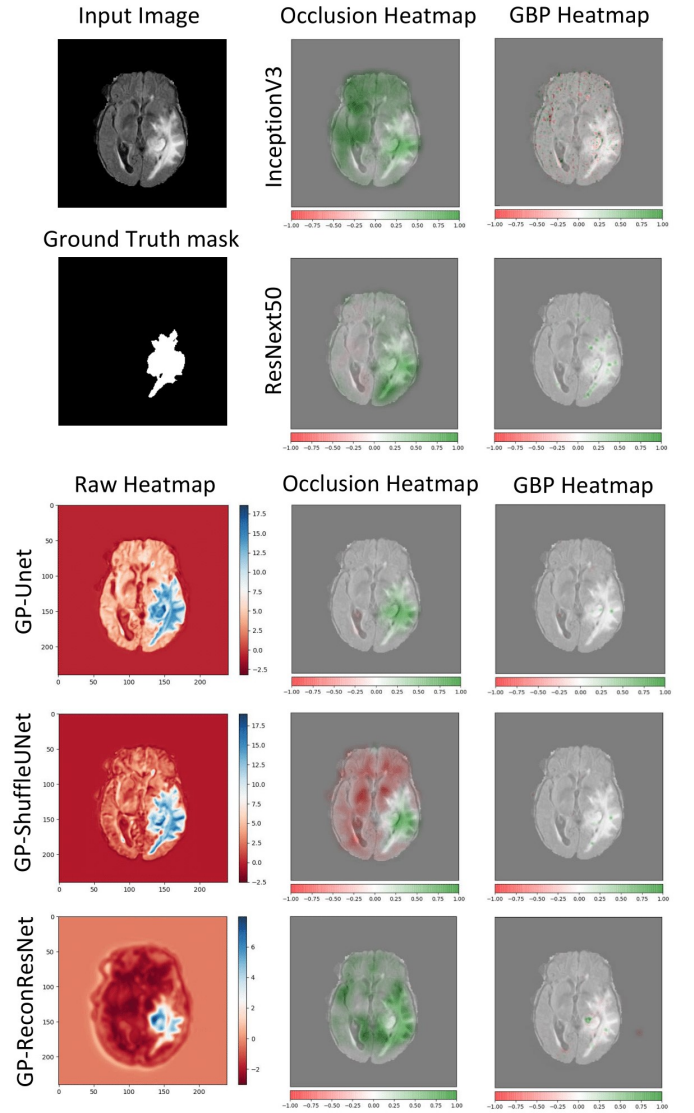


Figure 11: Example interpretability results of the GP- and non-GP models, correctly classified HGG (class 2). 1st column contains the input image, ground-truth mask, and the raw heatmaps of the GP-models. 2nd and 3rd columns contain the post-hoc interpretability attributions using the occlusion and the guided backpropagation (GBP) methods, respectively - overlaid as heatmaps on the input slices.

#### 4. Discussion

The proposed GP-models have demonstrated comparable classification performance with the non-GP baseline models. However, the advantage over the baseline non-GP models is their inherent explainability, which can increase trust of the decision-makers like clinicians over the opaque models. Most importantly, they have shown the capabilities for the task of performing brain tumour segmentation without training with any segmentation labels.

GP-models require more time in comparison to non-GP-models depending on the number of parameters, as shown in Table 1. More time is needed for GP-models because of the expanding part of the networks. Moreover, GP-ShuffleUNet, which has the highest number of parameters (26.4 M), consequently takes the longest time to train - ( $\sim 4$  days). Even though for the classification performance GP-UNet and GP-ShuffleUNet have achieved the same F1-score (0.93) on the second (BraTS) dataset, GP-ShuffleUNet got 0.94 accuracy while GP-UNet achieved 0.93. From the perspective of segmentation performance, GP-UNet yielded  $0.67 \pm 0.08$  Dice score while GP-ShuffleUNet got  $0.53 \pm 0.08$ . On the first dataset, GP-ShuffleUNet achieved lower scores compared to GP-UNet. The results show that as the GP-ShuffleUNet performs better when it is trained on a larger dataset and does not encounter additional difficulties such as different orientations mixed in the training set. Considering all these factors, GP-UNet should be preferred over GP-ShuffleUNet. On the second dataset, GP-ReconResNet has achieved the same accuracy as the GP-UNet (0.93) but had 0.01 lower F1-score (0.92), however, the segmentation performance of GP-ReconResNet has been lower than for GP-UNet - a median Dice score of  $0.60 \pm 0.06$ . Since GP-UNet has the least trainable parameters, reducing the chance of overfitting and superior overall performance, this can be considered the best performing model on the second dataset. However, on the first dataset, a different trend can be seen. GP-ReconResNet obtained 0.10 higher F1-score and accuracy than the GP-UNet model (0.95 and 0.85, respectively). Thus, it can be concluded that the GP-ReconResNet is more robust against variations in the dataset (different orientations) and requires less training data (performed better when the training set was considerably smaller). However, the results also indicate that the GP-ReconResNet model performs better when the dataset is more balanced. When the training dataset is larger, and all MRIs are in one orientation, GP-ReconResNet and GP-UNet result in a comparable performance.

The generated heatmaps bring two major advantages in favour of the GP-models - they make the models explainable, which can help decision-makers like radiologists to develop more trust in model outcomes. These classification models may thus be used as a decision support system to localise regions of interest, like in this case, tumours. By applying post-processing techniques to the heatmaps, the final segmentations are obtained, which are imperfect and have scope for improvements. However, given that no segmentation labels were used for training, and the segmentation was only trained in a weakly-supervised manner, a median Dice of  $0.67 \pm 0.08$  is promising.

By modifying the post-processing techniques, the segmentation performance might be improved further. The segmentation quality for all the methods was better for HGG than LGG (especially for GP-ReconResNet) - which can be attributed to the fact that the training data was highly imbalanced and was leaning more towards the HGG class. Hence, the results can be improved by reducing the imbalance in the dataset or employing further techniques to handle imbalanced datasets.

Table 5 compares the proposed GP-models to previously published glioma tumour grading models, which are using the BraTS dataset (but different versions). Since the models of this research are multi-class classifiers, test accuracy was calculated for the tumour-only subset of the data. The proposed models outperform the previous studies, with GP-ShuffleUNet receiving the highest score of 98.74%. On the plus side, the proposed 2D models, which are more resource-efficient, perform better even than the 3D models in the table, while the models here are also explainable by nature - giving them an advantage over the competition in terms of model transparency and explainability.

Finally, coming to the point of post-hoc interpretability techniques. The GP-models are inherently-explainable, but to understand the non-GP baselines, post-hoc interpretability techniques are required. Hence, a gradient-based technique - GBP and a feature-based technique - occlusion, were applied to all the models. For the GP-models, the interpretability results (also known as attention maps) were compared against the heatmaps of the networks - as they can be considered as a kind of "ground-truth". The models generally had reasonable attention maps, but there were some discrepancies and conflicting results between methods. However, assuming that the post-hoc methods are reliable (most of them agree with the networks' heatmaps), GP-UNet, GP-ShuffleUNet, and ResNext50 share similar outcomes, demonstrating proper tumour focal regions in both classes, followed by GP-ReconResNet, which has superior outcomes than InceptionV3. Even though InceptionV3 has the highest classification results, the attention maps show that positive and negative attributions are scattered compared to other models. They do not demonstrate the expected focus on the tumour for both tumour classes. A similar outcome can also be observed in a study of deep learning methods for COVID-19 classification using Chest-Xrays, where for certain models, the classification results are high, but post-hoc methods prove the models focus on different regions than the expected target(Chatterjee et al., 2020).

#### 5. Conclusion and Future Work

This paper presented three inherently-explainable deep learning models - GP-UNet, GP-ReconResNet, and GP-ShuffleUNet, and showed their applicability for the task of multi-class brain tumour classification. Segmentation and reconstruction models were converted into the GP-models by applying a global pooling layer before the final convolution layer of each of the models, and they were trained using classification labels instead of ground truth segmentations. During inference, the global pooling layer was disabled to obtain the models' localisation maps (raw heatmaps), while the pooling layer

was kept - to obtain the classification results. The segmentation results were obtained by post-processing the raw heatmaps without training the models using any segmentation labels. The models have achieved comparable performance with the non-explainable baseline classifiers (best accuracy for GP-models: 0.94, best accuracy for non-GP baselines: 0.95) while demonstrating their advantage in terms of explainability. All the GP-models resulted in better classification accuracy for the task of tumour classification (ignoring the tumour-free class) than the existing studies, while the best model secured 98.74% test accuracy. Moreover, this paper has shown the potential of using the GP-models to perform segmentation while being trained in a weakly-supervised manner using only the classification labels, resulting in the best median Dice score of  $0.67 \pm 0.08$ . The high accuracies, coupled with the heatmaps and the segmentations, have shown the potential of using these models as decision support systems.

## Acknowledgement

This work was in part conducted within the context of the International Graduate School MEMoRIAL at Otto von Guericke University (OVGU) Magdeburg, Germany, kindly supported by the European Structural and Investment Funds (ESF) under the programme "Sachsen-Anhalt WISSENSCHAFT Internationalisierung" (project no. ZS/2016/08/80646).

## References

- Abiwinanda, N., Hanif, M., Hesaputra, S.T., Handayani, A., Mengko, T.R., 2019. Brain tumor classification using convolutional neural network, in: Lhotska, L., Sukupova, L., Lacković, I., Ibbott, G.S. (Eds.), *World Congress on Medical Physics and Biomedical Engineering 2018*. Springer Singapore, Singapore. volume 68/1 of *IFMBE Proceedings*, pp. 183–189. doi:10.1007/978-981-10-9035-6\textunderscore{33}.
- Ayadi, W., Elhamzi, W., Charfi, I., Atri, M., 2021. Deep cnn for brain tumor classification. *Neural Processing Letters* 53, 671–700. doi:10.1007/s11063-020-10398-2.
- Badža, M.M., Barjaktarović, M.Č., 2020. Classification of brain tumors from mri images using a convolutional neural network. *Applied Sciences* 10, 1999. doi:10.3390/app10061999.
- Bakas, S., Reyes, M., Jakab, A., Bauer, S., Rempfler, M., Crimi, A., Shinhara, R.T., Berger, C., Ha, S.M., Rozycki, M., et al., 2018. Identifying the best machine learning algorithms for brain tumor segmentation, progression assessment, and overall survival prediction in the brats challenge. *arXiv preprint arXiv:1811.02629*.
- Barstugan, M., 2023. Classification of 3d-dwt features of brain tumours with svm. *Orclever Proceedings of Research and Development* 2, 39–49.
- Chatterjee, S., Breitkopf, M., Sarasaen, C., Yassin, H., Rose, G., Nürnberger, A., Speck, O., 2022a. Reconresnet: Regularised residual learning for mr image reconstruction of undersampled cartesian and radial data. *Computers in Biology and Medicine*, 105321doi:10.1016/j.compbimed.2022.105321.
- Chatterjee, S., Das, A., Mandal, C., Mukhopadhyay, B., Vipinraj, M., Shukla, A., Nagaraja Rao, R., Sarasaen, C., Speck, O., Nürnberger, A., 2022b. Torchsegeta: Framework for interpretability and explainability of image-based deep learning models. *Applied Sciences* 12, 1834. doi:10.3390/app12041834.
- Chatterjee, S., Nizamani, F.A., Nürnberger, A., Speck, O., 2022c. Classification of brain tumours in mr images using deep spatiotemporal models. *Scientific Reports* 12, 1–11. doi:10.1038/s41598-022-05572-6.
- Chatterjee, S., Saad, F., Sarasaen, C., Ghosh, S., Khatun, R., Radeva, P., Rose, G., Stober, S., Speck, O., Nürnberger, A., 2020. Exploration of interpretability techniques for deep covid-19 classification using chest x-ray images. *arXiv preprint arXiv:2006.02570*.
- Chatterjee, S., Sciarra, A., Dünnwald, M., Mushunuri, R.V., Podishetti, R., Rao, R.N., Gopinath, G.D., Oeltze-Jafra, S., Speck, O., Nürnberger, A., 2021. Shuffleunet: Super resolution of diffusion-weighted mris using deep learning, in: *2021 29th European Signal Processing Conference (EUSIPCO)*, IEEE. pp. 940–944. doi:10.23919/EUSIPCO54536.2021.9615963.
- Cho, H.h., Park, H., 2017. Classification of low-grade and high-grade glioma using multi-modal image radiomics features, in: *2017 39th Annual International Conference of the IEEE Engineering in Medicine and Biology Society (EMBC)*, IEEE. pp. 3081–3084.
- Deepak, S., Ameer, P., 2019. Brain tumor classification using deep cnn features via transfer learning. *Computers in biology and medicine* 111, 103345.
- Díaz-Pernas, F.J., Martínez-Zarzuela, M., Antón-Rodríguez, M., González-Ortega, D., 2021. A deep learning approach for brain tumor classification and segmentation using a multiscale convolutional neural network. *Healthcare (Basel, Switzerland)* 9. doi:10.3390/healthcare9020153.
- Dubost, F., Bortsova, G., Adams, H., Ikram, A., Niessen, W.J., Vernooij, M., Bruijne, M.D., 2017. Gp-unet: Lesion detection from weak labels with a 3d regression network, in: *International Conference on Medical Image Computing and Computer-Assisted Intervention*, Springer. pp. 214–221.
- Dutta, T.K., Nayak, D.R., Zhang, Y.D., 2024. Arm-net: Attention-guided residual multiscale cnn for multiclass brain tumor classification using mr images. *Biomedical Signal Processing and Control* 87, 105421.
- Ge, C., Gu, I.Y.H., Jakola, A.S., Yang, J., 2018. Deep learning and multi-sensor fusion for glioma classification using multistream 2d convolutional networks, in: *2018 40th Annual International Conference of the IEEE Engineering in Medicine and Biology Society (EMBC)*, IEEE. pp. 5894–5897.
- Hafeez, H.A., Elmagzoub, M.A., Abdullah, N.A.B., Al Reshan, M.S., Gilanie, G., Alyami, S., ul Hassan, M., Shaikh, A., 2023. A cnn-model to classify low-grade and high-grade glioma from mri images. *IEEE Access*.
- Irmak, E., 2021. Multi-classification of brain tumor mri images using deep convolutional neural network with fully optimized framework. *Iranian Journal of Science and Technology, Transactions of Electrical Engineering* 45, 1015–1036. doi:10.1007/s40998-021-00426-9.
- Jeong, B., Choi, D.S., Shin, H.S., Choi, H.Y., Park, M.J., Jeon, K.N., Na, J.B., Chung, S.H., 2014. T1-weighted flair mr imaging for the evaluation of enhancing brain tumors: Comparison with spin echo imaging. *Journal of the Korean Society of Magnetic Resonance in Medicine* 18, 151. doi:10.13104/jksmrm.2014.18.2.151.
- Jun Cheng, . brain tumor dataset. doi:10.6084/m9.figshare.1512427.v5.
- Kenny, E.M., Ford, C., Quinn, M., Keane, M.T., 2021. Explaining black-box classifiers using post-hoc explanations-by-example: The effect of explanations and error-rates in xai user studies. *Artificial Intelligence* 294, 103459. URL: <https://www.sciencedirect.com/science/article/pii/S0004370221000102>, doi:<https://doi.org/10.1016/j.artint.2021.103459>.
- Khawaldeh, S., Pervaiz, U., Rafiq, A., Alkhawaldeh, R.S., 2018. Noninvasive grading of glioma tumor using magnetic resonance imaging with convolutional neural networks. *Applied Sciences* 8, 27.
- Krizhevsky, A., Sutskever, I., Hinton, G.E., 2012. Imagenet classification with deep convolutional neural networks. *Advances in neural information processing systems* 25, 1097–1105.
- Latif, G., Butt, M.M., Khan, A.H., Butt, O., Iskandar, D.A., 2017. Multiclass brain glioma tumor classification using block-based 3d wavelet features of mr images, in: *2017 4th International Conference on Electrical and Electronic Engineering (ICEEE)*, IEEE. pp. 333–337.
- Laugel, T., 2020. Local Post-hoc Interpretability for Black-box Classifiers. Ph.D. thesis. Sorbonne Université, CNRS, LIP6, F-75005 Paris, France.
- Li, H., Li, A., Wang, M., 2019. A novel end-to-end brain tumor segmentation method using improved fully convolutional networks. *Computers in biology and medicine* 108, 150–160.
- Lloyd, C.T., Sorichetta, A., Tatem, A.J., 2017. High resolution global gridded data for use in population studies. *Scientific data* 4, 1–17.
- Madsen, A., Reddy, S., Chandar, S., 2021. Post-hoc interpretability for neural NLP: A survey. *CoRR abs/2108.04840*. URL: <https://arxiv.org/abs/2108.04840>, arXiv:2108.04840.
- Menze, B.H., Jakab, A., Bauer, S., Kalpathy-Cramer, J., Farahani, K., Kirby, J., Burren, Y., Porz, N., Slotboom, J., Wiest, R., et al., 2014. The multimodal



brain tumor image segmentation benchmark (brats). IEEE transactions on medical imaging 34, 1993–2024.

Mzoughi, H., Njeh, I., Wali, A., Slima, M.B., BenHamida, A., Mhiri, C., Mahfoudhe, K.B., 2020. Deep multi-scale 3d convolutional neural network (cnn) for mri gliomas brain tumor classification. Journal of Digital Imaging 33, 903–915.

Noor, M.B.T., Zenia, N.Z., Kaiser, M.S., Mahmud, M., Al Mamun, S., 2019. Detecting neurodegenerative disease from mri: A brief review on a deep learning perspective, in: Liang, P., Goel, V., Shan, C. (Eds.), Brain Informatics. Springer International Publishing, Cham. volume 11976 of *Lecture Notes in Computer Science*, pp. 115–125. doi:10.1007/978-3-030-37078-7\textunderscore12.

Pereira, S., Pinto, A., Alves, V., Silva, C.A., 2016. Brain tumor segmentation using convolutional neural networks in mri images. IEEE transactions on medical imaging 35, 1240–1251.

Razzak, M.I., Imran, M., Xu, G., 2018. Efficient brain tumor segmentation with multiscale two-pathway-group conventional neural networks. IEEE journal of biomedical and health informatics 23, 1911–1919.

Rehman, A., Naz, S., Razzak, M.I., Akram, F., Imran, M., 2020. A deep learning-based framework for automatic brain tumors classification using transfer learning. Circuits, Systems, and Signal Processing 39, 757–775.

Ronneberger, O., Fischer, P., Brox, T., 2015. U-net: Convolutional networks for biomedical image segmentation, in: International Conference on Medical image computing and computer-assisted intervention, Springer. pp. 234–241.

Shahzadi, I., Tang, T.B., Meriadeau, F., Quyyum, A., 2018. Cnn-ilstm: Cascaded framework for brain tumour classification, in: 2018 IEEE-EMBS Conference on Biomedical Engineering and Sciences (IECBES), IEEE. pp. 633–637.

Sultan, H.H., Salem, N.M., Al-Atabany, W., 2019. Multi-classification of brain tumor images using deep neural network. IEEE Access 7, 69215–69225. doi:10.1109/ACCESS.2019.2919122.

Szegedy, C., Vanhoucke, V., Ioffe, S., Shlens, J., Wojna, Z., 2016. Rethinking the inception architecture for computer vision, in: Proceedings of the IEEE conference on computer vision and pattern recognition, pp. 2818–2826.

Wong, S.C., Gatt, A., Stamatescu, V., McDonnell, M.D., . Understanding data augmentation for classification: when to warp? URL: <http://arxiv.org/pdf/1609.08764v2>.

Xie, S., Girshick, R., Dollár, P., Tu, Z., He, K., 2017. Aggregated residual transformations for deep neural networks, in: Proceedings of the IEEE conference on computer vision and pattern recognition, pp. 1492–1500.

Yang, Y., Yan, L.F., Zhang, X., Han, Y., Nan, H.Y., Hu, Y.C., Hu, B., Yan, S.L., Zhang, J., Cheng, D.L., et al., 2018. Glioma grading on conventional mr images: a deep learning study with transfer learning. Frontiers in neuroscience , 804.

Zhuge, Y., Ning, H., Mathen, P., Cheng, J.Y., Krauze, A.V., Camphausen, K., Miller, R.W., 2020. Automated glioma grading on conventional mri images using deep convolutional neural networks. Medical physics 47, 3044–3053.

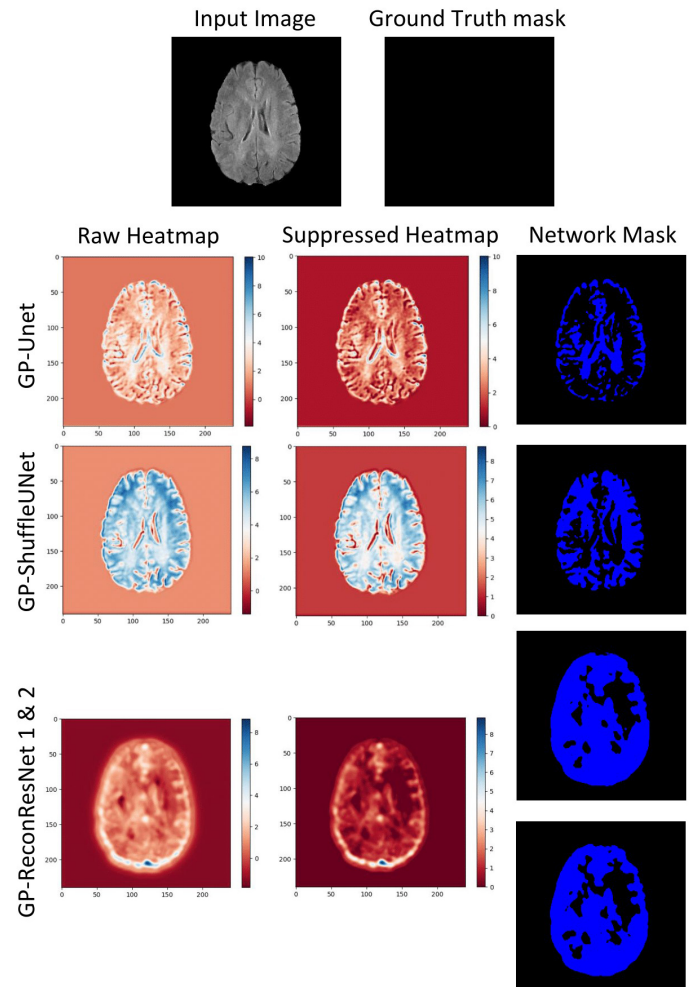


Figure .12: Example results of the GP-models' correctly classified tumour-free slices (class 0) from the BraTS 2020 dataset. 1st row is the input slice, the ground truth mask is used for comparison, and the rest of the rows are the models' outputs. For rest of the rows: 1st column contains the models' predictions known as the raw heatmaps, where the red areas influenced the classification outcome negatively, and the blue areas influenced the classification outcome favourably; 2nd column contains the suppressed heatmaps, where negative values are suppressed to obtain positive attributions only; 3rd column contains the networks' generated final masks = the suppressed heatmap + thresholding.